Title

Computational method for the optimization of quasimonoenergetic laser Compton x-ray sources for imaging applications.



Journal

Applied Optics, 61(6)

Authors

Effarah, Haytham

Reutershan, Trevor

Lagzda, Agnese

et al.

Publication Date

2022-02-20

DOI

10.1364/AO.444307

Peer reviewed

Published in final edited form as:

*Appl Opt*. 2022 February 20; 61(6): C143–C153. doi:10.1364/AO.444307.

# Computational method for the optimization of quasimonoenergetic Laser Compton X-ray sources for imaging applications

**Haytham H. Effarah**[1,2,*], **Trevor Reutershan**[1,2], **Agnese Lagzda**[3], **Yoonwoo Hwang**[3], **Fred V. Hartemann**[3], **C. P. J. Barty**[1,2,3]

[1]Department of Physics and Astronomy, University of California – Irvine, Irvine, CA, 92617, USA

[2]Beckman Laser Institute and Medical Clinic, University of California – Irvine, Irvine, CA 92612, USA

[3]Lumitron Technologies, Inc., 5201 California Ave, Suite 100, Irvine, CA, 92617, USA

## Abstract

The development of compact quasimonoenergetic X-ray radiation sources based on Laser Compton scattering (LCS) offers opportunities for novel approaches to medical imaging. However, careful experimental design is required to fully utilize the angle-correlated X-ray spectra produced by LCS sources. Direct simulations of LCS X-ray spectra are computationally expensive and difficult to employ in experimental optimization. In this manuscript, we present a computational method that fully characterizes angle-correlated LCS X-ray spectra at any endpoint energy within a range defined by three direct simulations. With this approach, subsequent LCS X-ray spectra can be generated with up to 200 times less computational overhead.

## 1. Introduction

Laser Compton scattering (LCS) produces X-rays with unique spectral-spatial distributions that are unlike those produced through bremsstrahlung and synchrotron radiation sources [1]. LCS produces X-rays by scattering laser photons off relativistic electrons. LCS X-ray sources can offer small energy bandwidths, i.e., quasimonoenergetic X-rays, and small effective source sizes that can enable high-precision imaging techniques not possible with bremsstrahlung sources [2]. While the monochromator output of synchrotron radiation sources can also produce high X-ray fluxes with energy bandwidths of less than 0.1% for high-resolution and low-dose imaging applications [3–7], the two primary limitations of synchrotron radiation are its facility-scale space requirements and its inverse relationship between X-ray flux and X-ray energy [8].

LCS sources offer the opportunity to produce quasimonoenergetic X-rays with room-scale, rather than facility-scale, space requirements. Additionally, while LCS sources have already

* effarahh@hs.uci.edu .

**Disclosures.** AL, YH, FVH: Lumitron Technologies, Inc. (I, E). CPJB: Lumitron Technologies, Inc. (I, E, P). HHE and TR declare no conflicts of interest.

been designed and built with X-ray fluxes and X-ray energies capable of preclinical medical imaging studies [9, 10], it has also been demonstrated both theoretically and experimentally that LCS light sources are capable of scaling to higher fluxes when tuned to produce X-rays at higher energies [11]. This direct relationship between flux and energy unlocks novel opportunities such as medical X-ray imaging with high-Z contrast agents [12], ultrahigh dose rate (FLASH) radiotherapy [13], and nuclear resonance fluorescence imaging, which itself has extended applications in nuclear security and non-destructive testing [14–16].

One medical imaging technique that quasimonoenergetic X-ray sources are naturally suited for is K-edge subtraction imaging, which utilizes the absorption line of a high-Z atom's inner shell electron to produce a strong differential X-ray absorption signal compared to those from biological tissues. Utilizing quasimonoenergetic X-rays above and below a contrast agent's K-edge can enhance regions that take up contrast agent more readily, as was first reported in 1983 at the Stanford Synchrotron Radiation Lightsource (SSRL) for rapid digital subtraction angiography (DSA) [17]. The extension of K-edge subtraction imaging from synchrotrons to LCS X-ray sources has been demonstrated with angiography [18], contrast-enhanced mammography [19], computed tomography [20], and fluoroscopy [21]. These preliminary experimental studies into the suitability of LCS X-ray sources for advanced medical imaging techniques have justified the development of more LCS X-ray sources capable of producing higher X-ray energies. They have also justified a more subtle analysis of the X-ray spectra generated from such sources. These initial studies approximated the LCS X-ray energy spectrum as the integrated spectrum over an entire region of interest (Fig 1.a), which may not fully take advantage of a unique property of LCS X-rays: an angle-correlated energy spectrum. The discontinuous nature of the atomic K-edge means that a precise understanding of the spatial distribution of LCS X-ray energies will enable the design of precision LCS imaging techniques.

For example, a LCS architecture employing a Gaussian electron beam in time and space and a horizontally polarized Gaussian laser pulse may produce distributions of X-ray flux, mean X-ray energy, and even local energy bandwidth that vary over the extent of the X-ray beam profile (Fig. 1). This angle-correlated distribution of X-rays further differentiates LCS radiation from commonly employed bremsstrahlung radiation in that the latter can often be considered to produce a distribution of X-ray energies that is preserved throughout its spatial extent. LCS X-rays have complicated spectral-spatial distributions but given the properties of the interacting electron beam and laser pulse, these complicated distributions are well described through simulation [22].

The characteristics of the interacting electron beam and laser pulse directly influence the Compton edge energy, divergence, local energy, local bandwidth, and flux distribution of the LCS X-ray output. However, conducting a detailed spectral analysis of LCS X-rays cannot be performed on the timescale of an imaging experiment. Thus, being able to reference simulated X-ray spectra for a given set of interaction conditions is required for precision experimental design. In applications that require quasimonoenergetic X-rays with strict bandwidth and field-of-view requirements, a set of simulated X-ray spectra with varying LCS interaction parameters should be consulted to identify optimal conditions. Simulations of LCS X-ray outputs have been shown to predict flux densities and spectral

distributions accurately but simulating the relativistic collisions of electrons and photons is computationally expensive. This is a severely limiting step in experimental optimization.

Because of this computational hurdle, there has been recent interest in describing the properties of LCS X-ray sources using convenient analytical forms [23, 24]. These descriptions show strong agreement with Monte Carlo simulations at small scattering angles and for a wide range of interaction conditions. Analytical descriptions of the spectral bandwidth and flux densities of an LCS source are invaluable for evaluating design benchmarks for the commissioning of new LCS sources, but the information they provide is insufficient for precision imaging applications. The advantage that direct simulation maintains over analytical approximations is the generation of detailed local X-ray spectra.

One study sought to retain the local spectral information of an LCS X-ray source by fitting simulated LCS X-ray data to a function that visually approximated the shape of the LCS X-ray energy spectrum over a field of view [25]. This allowed computationally efficient implementation into imaging simulation studies with some consideration of variation in local X-ray spectra. However, this previous work assumed that the shape of the local X-ray energy spectrum is the same at all scattering angles, which can be limiting in trying to produce realistic LCS X-ray spectra. An example of how the shape of the local X-ray energy spectrum can change with observation angle is illustrated in Fig. 2. Furthermore, and similarly for analytical approaches, radial symmetry must be assumed for X-ray intensity distributions, which precludes the use of polarized laser pulses.

This paper seeks to retain the detailed spectral-spatial information from direct simulations required for precision experimental design without the computational cost associated with generating the many spectra required for optimization. Instead of implementing a relativistic scaling factor ($1/\gamma$) to X-ray scattering angles, as is typically done in analytical approaches, this paper investigates how the local X-ray distribution at a specific scattering angle in the laboratory frame (i.e., a detector pixel) transforms as the energy of interacting electrons is varied. Instead of applying general physical scaling laws or making assumptions about the functional forms of local energy distributions, we instead use a data-driven approach to directly interpolate the transformation of local energy distributions between direct LCS simulation results.

This paper describes and evaluates a practical, computationally efficient approach to produce simulated LCS X-ray spectra over a range of Compton edge energies. Unlike previous work, this paper seeks to preserve the detailed local spectral information that is required for precision experimental design. For the remainder of this paper, we will refer to this approach to generating LCS X-ray spectra as *Compton FastFit*. The results and underlying methods of this paper will enable the precision design of experimental applications using LCS sources spanning medical imaging, non-destructive testing, and the interrogation of nuclear phenomena. The goals of this work are to (1) generate detailed LCS X-ray spectra with local deviations in mean energy and relative flux less than 1% in comparison with direct LCS simulations and to (2) decrease the computational time required to generate said spectra by more than two orders of magnitude.

This paper is organized as follows: First, the Laser Compton interaction will be briefly reviewed, followed by an explanation of the computational script used to generate simulated LCS X-ray spectra. Next, we will discuss our approach toward discretizing and fitting LCS X-ray spectra to a generalized functional form. We will then provide an evaluation of how reliably we can predict LCS X-ray spectra over a range of Compton edge energies. This experimentally translates to tuning the mean energy of an electron beam, a practical approach to tuning the energy of a linac-based LCS source. Finally, we will use our interpolation technique to determine which combinations of X-ray beam apertures and Compton edge energies are necessary to maximize X-ray output within an energy bandwidth constraint to demonstrate the utility of *Compton FastFit*.

## 2. Model and Computational Method

### 2.1 Modeling of Laser Compton sources

The spectral-spatial distribution of X-rays produced by a relativistic laser Compton source is dependent on the interaction conditions between a laser pulse and a relativistic electron beam. Within the moving frame of the electron, the incoming laser field is Doppler upshifted. In the lab frame of the observer, the resulting Compton-scattered radiation is additionally Doppler upshifted. For sufficiently energetic electrons, the resulting doubly Doppler upshifted energy of the relativistic Compton-backscattered photons can easily fall into the X-ray regime. To an observer in the laboratory rest frame, the results of this process may appear somewhat confusingly to be the result of an “inverse” physical process in which higher energy photons are produced from lower energy incident photons. However, within the rest frame of the electron, the underlying physics is simply that of traditional Compton scattering between photons and electrons.

The exact energy of a Compton-scattered X-ray, $E_\gamma$, emerging from a photon collision with a relativistic electron is given by:

$$E_\gamma = \frac{\gamma - \sqrt{\gamma^2 - 1}\cos\phi}{\gamma - \sqrt{\gamma^2 - 1}\cos\theta + k_0 \lambda\!\!\!^{-}_c (1 - \cos\theta\cos\phi + \cos\psi\sin\theta\sin\phi)} E_L \quad (1)$$

where $\gamma$ is the electron’s Lorentz factor, $k_0$ is the wave number of the incident photon, $\lambda\!\!\!^{-}_c$ is the reduced Compton wavelength of the electron, $E_L$ is the incident photon energy, $\phi$ is the angle between the incident electron and photon, $\theta$ is the angle between the incident electron and scattered photon, and $\psi$ is the angle between incident and scattered photons. In the simplified case of a head-on collision, where $\phi = \pi$, and for small observation angles, where $\sin\theta \approx \theta$, the equation can be approximated to be

$$E_\gamma \approx \frac{4\gamma^2}{1 + \gamma^2\theta^2 + 4\gamma k_0 \lambda\!\!\!^{-}_c} E_L . \quad (2)$$

This approximation is made under the assumption of a single photon colliding head-on with a single electron at small scattering angles. As $\theta \to 0$, $E_\gamma \to E_{CE}$, where $E_{CE}$ is defined as the Compton edge energy. To produce realistic distributions of Compton-scattered

X-rays, the beam characteristics of both an electron beam and interaction laser must be considered, along with the Compton scattering cross sections between participating electrons and laser photons. For the distributions in this paper, X-ray beam spectra and beam profiles are simulated using a Mathematica script originally developed and experimentally validated by F.V. Hartemann, S. Wu and Y. Hwang at the Lawrence Livermore National Laboratory (LLNL) [26] and adapted for use by Lumitron Technologies, Inc. The script calculates resulting Compton X-ray flux, spectrum, and spatial distribution for a simulated interaction of an electron beam and laser pulse. This script is based on physics and processes that have been previously described [27, 28].

First, a 75 MeV electron beam with one hundred thousand particles is simulated using General Particle Tracer (GPT) code. The phase space values of this electron beam are then modified within the Mathematica script to fit desired beam parameters (electron beam energy, divergence, spot size, etc.). In this paper, the electron beam has a normalized x- and y-emittance of about 0.15 and 0.12 respectively, with an interaction spot size of about 5 μm. In linac-based LCS sources, the normalized emittance can be assumed to stay constant as the electron beam energy is scaled and the laser Compton focal spot size can be maintained via adjustment of the magnetic focusing optics [29].

The laser pulse is modelled as a Gaussian beam. Hence, laser pulse bandwidth and divergence effects are not simulated within this script. Previous analyses have indicated that in a typical LCS arrangement that does not employ ultrafast (femtosecond) laser pulses, the bandwidth and divergence of the laser pulse are not a significant contributor to changing the LCS X-ray spectrum when compared to the emittance and spot size of the interacting electron beam [11]. The Mathematica script assumes laser pulse widths on the order of picoseconds, in which this approximation is valid. The amplitude of the focused laser pulse is always less than the electric field amplitude of the relativistic electron beam, allowing us to assume the linear Compton scattering regime.

After defining our interaction conditions, a discrete grid of observation angles ($\theta_x$ and $\theta_y$) in horizontal and vertical planes is set up. At each grid point, for each electron beam particle, the script calculates the Compton-scattered X-ray energy and number of photons scattered at that energy. The energy and differential cross sections of Compton-scattered X-rays are calculated using energy-momentum conservation and the Klein-Nishina formula for linearly polarized photons. The interaction probability between the electron and laser beams is calculated by integrating the photon density along the ballistic trajectory of the electron, which is then multiplied by the Compton scattering cross-section to give the number of photons within the solid angle at each grid point. Finally, contributions of all electron particles for all grid points are summed up.

Laser Compton X-ray distributions produced in this way are then used as the input for the *Compton FastFit* algorithm for fitting and interpolation. It is important to note that *Compton FastFit* is agnostic to the Laser Compton simulation used, so long as the LCS simulation output can be expressed as a grid of observation angles with information about the spatial and energy distributions of the Compton-scattered X-rays.

### 2.2 Spectral-spatial fitting and interpolation using Compton FastFit

The input of the *Compton FastFit* interpolation algorithm requires data that describe the distribution of Compton-scattered X-rays in terms of both scattering angle and photon energy generated from a Laser Compton Scattering (LCS) simulation code. We will refer to these file inputs as anchor distributions as they will serve as the anchors for our interpolations.

After anchor distributions have been loaded, *Compton FastFit* then fits polynomial expressions to the local energy distribution at each observation angle ($\theta_x$, $\theta_y$) using Vandermonde matrices, or, in regions where the local bandwidth is especially small ($\theta_x$, $\theta_y \approx 0$ mrad), nonlinear least-squares fitting. The polynomial fits are then rescaled to match the relative X-ray flux at that observation angle. We refer to these functional approximations as anchor-fits. Paired with these anchor-fits are also bounds over the range of energies produced at each observation angle, which appropriately truncate the polynomial function at its nearest zeros on each side of the distribution. The dimensions of the anchor-fit matrix generated is determined by the observation angle binning provided in the anchor distributions. Thus, at this stage, each anchor distribution can be approximated as an anchor-fit of dimensions ($m$, $n$, $o$) where $m$ and $n$ indicate the number of $\theta_x$ and $\theta_y$ bins respectively, and $o$ indicates the number of polynomial coefficients employed to generate the functional approximation of the local energy distributions. While the polynomial order can be easily altered by the user, we have used eighth degree polynomials here (i.e., $o = 9$). While this approach is not theoretically limited to polynomials, we found that using polynomials allowed for very efficient fitting and interpolation, even with many coefficients.

Once we have produced anchor-fit counterparts from anchor distributions, we then evaluate goodness-of-fit by comparing two parameters between our anchor-fits and anchor distributions at each observation angle: flux density and mean energy. We then calculate the mean absolute percentage error (MAPE) for each parameter over the entire set of considered observation angles to provide a quantitative metric for the fitted and interpolated spectra.

After producing polynomial-fitted counterparts for our original anchor distributions, we examine how X-ray flux and mean energy change between anchor distributions at each observation angle. Based on the transformation of flux and mean energy at each observation angle as $E_{CE}$ ranges from 20 keV to 100 keV, we can qualitatively see that parameters increase in a way that can be well-approximated as quadratic (Fig. 3). Since our field of view only includes small scattering angles and since we assume a head-on collision between electrons and laser photons, we find that Eq. (2) describes the mean energy distributions in Fig. 3c and Fig. 3d well. For generality, however, we still create a quadratic interpolation map for both mean energy and relative flux at each observation angle. These mappings allow *Compton FastFit* to *rescale* local energy distributions appropriately as Compton edge energy is varied.

To *reshape* the local energy distributions as a function of $E_{CE}$, we overlay a quadratic interpolation map over three anchor-fits ($E_{CE} = 20$ keV, 60 keV, 100 keV) of dimensions ($m$, $n$, $o$) for each polynomial coefficient. This is because polynomial coefficients were also observed to vary over $E_{CE}$ in a way that was well-approximated by quadratic functions.

Thus, our final interpolation map is a matrix with dimensions ($m$, $n$, $o$, 3). This interpolation map describes how each polynomial coefficient varies at each observation angle while $E_{CE}$ is tuned. To maintain appropriate local energy bandwidths, the energy bounds are also quadratically interpolated and carried through as constraints for the polynomials generated by the interpolation map.

To evaluate this approach for the rapid generation of LCS X-ray spectra, we compare these predicted X-ray spectra with those generated using the Mathematica script described in the previous section (Section 2.1). To scan over a range of Compton-edge energies, as we do in Section 3.3 and Section 3.4, we simply loop over an iteration of predicted Laser Compton X-ray output distributions. We embed functions in these iterative loops to calculate properties of interest that are then plotted to identify X-ray aperture and $E_{CE}$ pairs that optimize our properties of interest.

Producing a single LCS X-ray distribution using the Mathematica script described in Section 2.1 requires 16 CPU minutes on one core of an Intel® Core™ i5-8279U Processor. Producing the initial *Compton FastFit* interpolation map requires 2 CPU minutes (regardless of anchor function CPU time). After the interpolation map has been generated, only 5 CPU seconds are required to produce an LCS X-ray distribution from the interpolation map. As *Compton FastFit* still requires three anchor functions to initialize (48 CPU minutes in our case), the utility of this technique from the standpoint of computation time is best realized in applications where many LCS X-ray spectra need to be generated to identify optimal LCS interaction parameters. All *Compton FastFit* code was written and tested in MATLAB R2021a and can be accessed with explicit instructions on how to generate the data that will be presented and discussed in this paper [30, 31].

## 3. Simulation Results and Discussion

### 3.1 Producing anchor-fits from LCS anchor distributions

We first seek to evaluate how well the anchor distributions provided by direct LCS simulation can be described as matrix of polynomials, which we refer to as anchor-fits. This evaluation is carried out through a pixel-by-pixel image subtraction between anchor distributions and their respective anchor-fits. Image subtraction results between an anchor distribution with $E_{CE}$ = 60 keV and its anchor-fit is shown in Fig. 4. The absolute percentage error (APE) is calculated at each observation angle for both X-ray flux and mean energy. Calculations of the mean absolute percentage error (MAPE) are inset in 4(a) and 4(b). The anchor-fit was produced using a matrix of eighth degree polynomials.

In Fig. 4(a), the flux image subtraction at each observation angle is essentially non-existent, reflected by the order $10^{-14}$ percent errors at each observation angle. This is present by design, as polynomial functions at each observation angle are re-scaled such that the flux exactly matches that of the anchor distribution. Our decision to explicitly constrain flux while fitting our anchor distributions is that in a quasimonoenergetic X-ray spectrum, the flux is the most important determiner of dose. Thus, trying our best to maximize fidelity in flux reproduction will make radiation dose simulations using these spectra more reliable.

In Fig. 4(b) we see small deviations in mean energy, with the largest deviations near the edges of the image where the total number of scattered X-rays is lowest. Regions of higher X-ray flux (central) tend to have their mean energies more accurately reproduced in the functional approximation, though throughout the distribution the absolute percentage error (APE) in mean energy prediction is at most just above 0.02%.

Based on our goal of minimizing local deviations in mean energy and relative flux to less than 1% between spectra generated from *Compton FastFit* and traditional LCS simulations, the direct fitting of LCS energy spectra using a simple array of polynomials is well within our benchmark for success. The generality of polynomial functions and our separation of the X-ray spectrum into discrete observation angles allows for the accurate description of the shape of local X-ray distributions. As illustrated in Fig. 2, and again later in Fig. 5, assuming a static functional form for all observation angles would lead to inaccurate reproductions of local X-ray spectra.

### 3.2 Interpolation of Laser Compton X-ray distributions while varying $E_\gamma$

After expressing the anchor distributions generated from direct LCS simulation as anchor-fits, we then produce a discretized interpolation map for each observation angle that slightly deforms local polynomial functions to smoothly transition between anchor-fits. These gradually morphing polynomials are then remapped onto the relative flux and mean energy values that correspond to the appropriate value of $E_{CE}$ (Fig. 3).

To investigate the reliability of this interpolation approach, we produced an interpolation map using anchor functions with $E_{CE}$ = 20 keV, 60 keV, 100 keV and produced an interpolated LCS X-ray distribution at $E_{CE}$ = 80 keV. We evaluated how reliable this interpolated LCS X-ray spectrum was by comparing it to a distribution produced using direct LCS simulation. We then use the same image subtraction technique employed in Fig. 4. Image subtraction plots and MAPE insets are shown in Fig. 5.

Unlike the flux image subtraction in Fig. 4 between anchor distributions and anchor-fits, we cannot make any explicit constraints on interpolated spectra. This causes an expected increase in flux APE in Fig. 5(a) as we attempt to interpolate to new values of $E_{CE}$. However, our MAPE is still well below 1% over the entirety of the image, and the largest APEs are at the largest observation angles. At these large observation angles, relative X-ray flux is lowest. Even then, the largest APE values are only about 1.5% at the fringes of the region of interest.

In Fig. 5(b), we see an increase in MAPE by about an order of magnitude when compared with Fig. 4(b). Even so, the MAPE in mean energy prediction is less than a fraction of a percent. Expectedly, the worst fits occur at the largest observation angles, where a lower relative flux will decrease our ability to accurately predict mean energy since there is a smaller relative population of X-ray photons at that observation angle to sample from. At the largest observation angles, the APE does not reach over 0.2% between direct LCS simulation and interpolated predictions. If direct LCS simulation is performed with a sufficiently large sampling of Compton-scattered particles at a given observation angle,

we believe that mean energy should naturally remain well-predicted using this interpolation technique.

To better visualize how our interpolated polynomials are fitting at each observation angle, we examine the local energy distributions at two observation angles from Fig. 5 for both the *Compton FastFit*-interpolated and direct LCS simulation-generated X-ray spectra (Fig. 6). These polynomial fits are typical over the entire range of observation angles of interest and demonstrate qualitatively that there are no regions of unusual deviation from local energy distributions in our anchor distributions, even after interpolation.

To illustrate the reliability of *Compton FastFit* over a range of interpolated spectra, MAPE analysis was repeated at different $E_{CE}$ values using the same interpolation map. The resulting MAPE for flux and mean energy are recorded in Table 1. In general, MAPE is lower for interpolated spectra with $E_{CE}$ closer to those of the anchor distributions. The MAPE also tends to be larger for lower energies (especially for flux) because given the same direct LCS simulation conditions, more X-rays are scattered outside of observation angles of interest, leading to a noisier anchor distribution and thus a less reliable fit. In other words, of the three anchor distributions employed, we expect $E_{CE}$ = 20 keV to be the noisiest. Even so, the calculated MAPE values are below our 1% benchmark for success with respect to flux, and less than 0.1% in mean energy.

Based on these results, we believe that *Compton FastFit*'s use of polynomial approximations and quadratic interpolations is an effective, reliable, and computationally efficient approach to scanning through different $E_{CE}$ values for a given LCS X-ray source configuration. This approach can be used to optimize LCS source settings for a given imaging application. We also note here that these results are only tested in the linear Compton regime (where the amplitude of the interaction laser pulse is lower in magnitude than the amplitude of the electric field of the electron beam), the regime where all currently commissioned LCS X-ray sources operate for imaging applications.

Furthermore, we only validate the use of this interpolation map when the employed anchor functions have sufficient X-rays scattered to them. Typically, as $E_{CE}$ increases, more X-rays are strongly forward scattered near $\theta = 0$, reducing the relative flux at larger observation angles. Using *Compton FastFit* in its presented form at higher energies will require a reduced range of observation angles. Although not explicitly discussed in this paper, extrapolation to energies outside of the range of anchor distributions is possible if there is a sufficiently large flux at each observation angle.

We also believe that it is both possible, and a benefit to the application of LCS X-ray sources, to extend these interpolations to other LCS interaction parameters like electron beam emittance and interaction spot size. Future work by the authors intends to explore these other LCS beam parameters to provide more optimizable variables for imaging applications. To better scan over multiple parameters simultaneously, we could further generalize how we approximate spectra and generate interpolation maps through machine-learned approaches. However, we believe that interpolating over LCS interaction parameters

that are conveniently tunable at LCS X-ray sources is of the most immediate practical interest.

### 3.3 Application: circular aperture optimization

To test the utility of *Compton FastFit*, we presented the simple task of optimizing $E_{CE}$ and the radius of a circular beam aperture to maximize X-ray flux passing through the aperture. In a simplified version of a constraint that could be used in designing a K-edge subtraction imaging experiment, X-rays are constrained to have energies within a bandwidth of interest. For this illustrative problem, we define a "good" X-ray energy as $E_{good} \equiv 72$ keV ± 2% X-rays of any other energy are labeled as having an energy $E_{bad}$. We define a threshold of acceptance such that 80% of the X-ray flux through the aperture is attributed to X-rays with energy $E_{good}$ Using *Compton FastFit* and the anchor distributions described previously at $E_{CE} = 20$ keV, 60 keV, 100 keV, we interpolate LCS X-ray spectra with $E_{CE}$ ranging from 70 keV to 80 keV at a spacing of 0.2 keV. We also scan through circular aperture radii ranging from 0.1 mrad to 5 mrad at a resolution of 0.1 mrad and calculate the difference between "good" and "bad" X-ray flux, normalized to the total X-ray flux within the aperture. This metric allows for an intuitive visualization of the relative flux of "good" X-rays, $N_{good}$, where a metric value of 1 indicates that all X-rays lie within our energy bandwidth constraint and a value of −1 indicates that all X-rays lie outside of our energy bandwidth constraint (Fig. 7).

From Fig. 7, we see that there is a clear delineation of aperture radius and $E_{CE}$ combinations that satisfy our constraint, and we can select the combination that maximizes X-ray flux with said constraint by maximizing aperture radius within the 0.8 contour. The result of this optimization is reasonable, as 72 keV + 2% = 73.4 keV, which is very near our interpolated prediction for the ideal value of $E_{CE} = 73.6$ keV. From Eq. 2, we can see that the X-rays with the highest energies produced through LCS are completely forward scattered, or in other words, scattered to $\theta = 0$. Thus, for a circular aperture, it is reasonable that tuning our Compton edge, $E_{CE}$, to a value that lies outside of the upper limit of an energy constraint will begin to introduce "bad" X-rays in our aperture and thus rapidly increase the value of $N_{bad}$ for small beam aperture radii. To validate this result, we produced multiple LCS X-ray spectra using direct LCS simulations at $E_{CE}$ values around 73.6 keV and set circular apertures to 2.8 mrad to see how well our interpolated optimization plan matches the results of direct LCS simulation (Fig. 8).

From Fig. 8 we see a remarkably accurate prediction of our metric's value for corresponding values of aperture radius and $E_{CE}$. Through simple polynomial functional approximations and a quadratic interpolation map we can obtain practical information about a Laser Compton source that can be used to optimize interaction parameters and aperture design. The total computational time required from *Compton FastFit* to produce the LCS X-ray spectra required for this analysis was 54 CPU minutes; 48 CPU minutes to produce three anchor distributions, 2 CPU minutes to produce the interpolation map, and then only 4 CPU minutes to produce 50 LCS X-ray spectra. Producing the same spectra using just LCS interaction code would require 800 CPU minutes, or just over 13 CPU hours.

This approach to LCS parameter optimization may be especially useful in designing K-edge imaging experiments with LCS X-ray sources. Maximizing X-ray flux will minimize image acquisition time, while constraining bandwidth will maximize image contrast per unit dose imparted upon the patient. In the application of this code to a real K-edge imaging example, one could easily define their bandwidth acceptance metric based on which X-ray energies maximize the differential absorption response from the contrast agent. This differential absorption response will be unique to the geometry and composition of the sample.

### 3.4 Application: annular aperture optimization

As a slightly more complicated example compared to the previous section (Section 3.3), we have generalized our search for a combination of aperture radius and Compton edge energy, $E_{CE}$, to consider either circular or annular apertures. In general, with circular apertures, one must reduce the radius of the aperture to minimize the energy bandwidth of the LCS X-ray output, as X-ray energy decreases with radial symmetry as the observation angle increases (see Fig. 1). However, because of this predictable radial energy dependence, one could employ annular apertures to take advantage of the relatively small local bandwidth at a given radial scattering angle (Fig. 1.b). Since the tuning of $E_{CE}$ for any LCS X-ray source has yet to be accomplished on the experimental timescale [18–21, 32, 33], alternative approaches to rapidly changing the energy spectrum of an LCS X-ray source are of practical interest.

We define an annular aperture here to have an inner radius, $r_i$, and an outer radius, $r_o$, such that only X-rays scattered to observation angles that subtend the solid angle contained between the two radii are considered. In this example, $r_i$ is allowed to have values down to $r_i = 0$ mrad whereas $r_o$ has a minimum allowed value of $r_o = 0.1$ mrad. We optimize to the same metric as in Section 3.2, seeking to find combinations of $E_{CE}$ and aperture geometry that maximize the X-ray flux that passes through the aperture given that at least 80% of the X-rays are of energies 72 keV ± 2%. To condense the results of our optimization, we report the $r_o$ and $r_i$ combination that resulted in the largest X-ray flux for each value of $E_{CE}$. We also report the X-ray flux, $N_{total}$, that passed through the optimal aperture for each value of $E_{CE}$ (Fig. 9). All other combinations of $r_o$ and $r_i$ at a given value of $E_{CE}$ either resulted in a lower X-ray flux or did not conform to the previously stated X-ray energy constraint.

From Fig. 9, we see the range of $E_{CE}$ values that have any possibility of satisfying our Xray energy constraint. In agreement with the $(N_{good} - N_{bad})/N_{total} = 0.8$ contour in Fig. 6, satisfying the constraint with a circular aperture ($r_i = 0$) is only possible at $E_{CE}$ values ranging from about 71 keV to just below 74 keV. At values below 71 keV, no X-rays are being generated through the Laser Compton interaction that satisfy our X-ray energy constraint. However, as $E_{CE}$ is tuned above 74 keV, the inclusion of annular aperture options allows us to block central X-rays which in turn allows us to decrease the overall energy bandwidth of X-rays passing through the aperture. For example, at $E_{CE} = 75$ keV, the use of an annular aperture with $r_i = 2.3$ mrad and $r_o = 3.4$ mrad will result in an X-ray spectrum that satisfies the energy constraint with only a 33% decrease in total flux when compared to the ideal circular aperture that maximizes X-ray flux at $E_{CE} = 73.6$ keV and $r_o = 2.8$ mrad. As with the previous example, once anchor distributions and the interpolation map were initialized, only 4 CPU minutes were required to generate the LCS X-ray spectra for this

analysis using *Compton FastFit*. It is important to note that new anchor distributions only need to be produced when LCS interaction parameters other than $E_{CE}$ have been altered, e.g., electron beam emittance, interaction spot size, laser pulse intensity.

In an imaging application that requires the use of two energies like K-edge subtraction imaging, being able to quickly change the spectral content of the LCS X-ray output can facilitate experimentation. An analogous approach to rapidly changing the LCS X-ray spectrum has been demonstrated using filters, but the annular aperture approach may preserve X-ray flux and energy bandwidth at the cost of requiring sample scanning to ensure imaging of the same sample coordinates. Another promising approach to rapidly tuning $E_{CE}$ has been proposed and recently experimentally tested, which instead changes the laser source or laser interaction angle with respect to an electron beam through fine adjustments in an optical cavity [34, 35]. Regardless of the ultimate approach employed in LCS energy tuning, the rapid and accurate generation of simulated LCS X-ray spectra with varying $E_{CE}$ facilitates the evaluation of experimentally relevant spectral properties.

## 4. Conclusion

In this paper we have described and implemented a computationally efficient, data-driven technique to generate LCS X-ray spectra with detailed local energy information and interpolate said LCS X-ray spectra through simulating the energy tuning of an electron beam in a linear accelerator (changing $E_{CE}$). By constraining the relative X-ray flux throughout a collection of observation angles, we observe good agreement between the properties of X-ray spectra generated through a direct LCS simulation and interpolations from *Compton FastFit*. Furthermore, in terms of CPU time, generating an X-ray spectrum using the *Compton FastFit* interpolation map is about 200 times more rapid than generating the same X-ray spectrum through detailed LCS interaction code. We demonstrate the utility of *Compton FastFit* by finding the optimal $E_{CE}$ and aperture geometry for a given energy bandwidth constraint, an optimization approach that can be directly applied to bandwidth-dependent imaging experiments. The underlying assumption of *Compton FastFit* in its presented form is that scanning over mean electron energy does not impact other electron beam parameters, e.g., emittance, energy spread and focal spot size. This assumption is valid for linearly accelerated electrons or for electron storage ring architectures in which the Compton edge is tuned through means that will not affect the electron beam emittance.

While *Compton FastFit* relies on spatial discretization to interpolate between LCS X-ray energy spectra, an alternative approach to simulating mean electron energy variation could be to use a relativistic coordinate system, rather than a rectilinear one. The local energy distributions at a given $E_{CE}$ are adjusted to new coordinates as the Lorentz factor of the accelerated electron beam changes. This adjustment could then be projected onto a rectilinear coordinate system to reconstruct the new local energy distributions at each observation angle in the lab frame. Through the underlying principle of discretizing observation angles, there are many opportunities to conveniently describe the X-ray spectra of these rapidly emerging sources. We believe that this approach to approximating LCS X-ray spectra will prove to be an invaluable tool in optimizing LCS sources for precision imaging applications whose parameters of interest are dependent on X-ray energy, flux, and

local bandwidth (e.g., K-edge subtraction imaging, medical CT, phase-contrast imaging, non-destructive material testing, nuclear resonance fluorescence imaging, and isotope detection).

## Acknowledgments.

TR and HHE received partial training funding through the NIH T32 grant listed above. TR and HHE contributed equally to the manuscript. The authors would like to thank Eric Carl Nelson and Kyle Daane Chesnut for their helpful discussions.

### Funding.

National Institutes of Health (T32GM008620).

## Data availability.

Data underlying the results presented in this paper are available in Ref. [31]. All code used to generate the figures in this paper are available in Ref. [30] and can be used with the provided data to recreate all presented results. Laser Compton scattering interaction code used to produce anchor functions is not publicly available at this time but is available upon reasonable request.

## References

1. Hartemann FV, Tremaine AM, Anderson SG, Barty CPJ, Betts SM, Booth R, Brown WJ, Crane JK, Cross RR, Gibson DJ, Fittinghoff DN, Kuba J, Sage GPLE, Slaughter DR, Wootton AJ, Hartouni EP, Springer PT, Rosenzweig JB, and Kerman AK, “Characterization of a bright, tunable, ultrafast Compton scattering X-ray source,” Laser and Particle Beams 22, 221–244 (2004).
2. Kulpe S, Dierolf M, Günther B, Brantl J, Busse M, Achterhold K, Pfeiffer F, and Pfeiffer D, “Spectroscopic imaging at compact inverse Compton X-ray sources,” Physica Medica 79, 137–144 (2020). [PubMed: 33271418]
3. Saukko AEA, Turunen MJ, Honkanen MKM, Lovric G, Tiitu V, Honkanen JTJ, Grinstaff MW, Jurvelin JS, and Toyras J, “Simultaneous Quantitation of Cationic and Non-ionic Contrast Agents in Articular Cartilage Using Synchrotron MicroCT Imaging,” Sci Rep 9, 7118 (2019). [PubMed: 31068614]
4. Piai A, Contillo A, Arfelli F, Bonazza D, Brombal L, Assunta Cova M, Delogu P, Di Trapani V, Donato S, Golosio B, Mettivier G, Oliva P, Rigon L, Taibi A, Tonutti M, Tromba G, Zanconati F, and Longo R, “Quantitative characterization of breast tissues with dedicated CT imaging,” Physics in Medicine and Biology 64(2019).
5. Longo R, Arfelli F, Bonazza D, Bottigli U, Brombal L, Contillo A, Cova MA, Delogu P, Di Lillo F, Di Trapani V, Donato S, Dreossi D, Fanti V, Fedon C, Golosio B, Mettivier G, Oliva P, Pacile S, Sarno A, Rigon L, Russo P, Taibi A, Tonutti M, Zanconati F, and Tromba G, “Advancements towards the implementation of clinical phase-contrast breast computed tomography at Elettra,” J Synchrotron Radiat 26, 1343–1353 (2019). [PubMed: 31274463]
6. Labriet H, Nemoz C, Renier M, Berkvens P, Brochard T, Cassagne R, Elleaume H, Estève F, Verry C, Balosso J, Adam JF, and Brun E, “Significant dose reduction using synchrotron radiation computed tomography: first clinical case and application to high resolution CT exams,” Scientific Reports 8, 12491 (2018). [PubMed: 30131501]
7. Fedon C, Rigon L, Arfelli F, Dreossi D, Quai E, Tonutti M, Tromba G, Cova MA, and Longo R, “Dose and diagnostic performance comparison between phase-contrast mammography with synchrotron radiation and digital mammography: a clinical study report,” J Med Imaging (Bellingham) 5, 013503 (2018). [PubMed: 29430473]

8. Stevenson AW, Crosbie JC, Hall CJ, Hausermann D, Livingstone J, and Lye JE, "Quantitative characterization of the X-ray beam at the Australian Synchrotron Imaging and Medical Beamline (IMBL)," J Synchrotron Radiat 24, 110–141 (2017). [PubMed: 28009552]
9. Eggl E, Dierolf M, Achterhold K, Jud C, Günther B, Braig E, Gleich B, and Pfeiffer F, "The Munich Compact Light Source: initial performance measures," Journal of Synchrotron Radiation 23, 1137–1142 (2016). [PubMed: 27577768]
10. Gunther B, Gradl R, Jud C, Eggl E, Huang J, Kulpe S, Achterhold K, Gleich B, Dierolf M, and Pfeiffer F, "The versatile X-ray beamline of the Munich Compact Light Source: design, instrumentation and applications," J Synchrotron Radiat 27, 1395–1414 (2020). [PubMed: 32876618]
11. Hartemann FV, Brown WJ, Gibson DJ, Anderson SG, Tremaine AM, Springer PT, Wootton AJ, Hartouni EP, and Barty CPJ, "High-energy scaling of Compton scattering light sources," Physical Review Accelerators and Beams 8, 100702 (2005).
12. Chi Z, Du Y, Huang W, and Tang C, "Linearly polarized X-ray fluorescence computed tomography based on a Thomson scattering light source: a Monte Carlo study," Journal of Synchrotron Radiation 27, 737–745 (2020). [PubMed: 32381776]
13. Montay-Gruel P, Bouchet A, Jaccard M, Patin D, Serduc R, Aim W, Petersson K, Petit B, Bailat C, Bourhis J, Bräuer-Krisch E, and Vozenin M-C, "X-rays can trigger the FLASH effect: Ultra-high dose-rate synchrotron light source prevents normal brain injury after whole brain irradiation in mice," Radiother Oncol 129, 582–588 (2018). [PubMed: 30177374]
14. Pruet J, McNabb DP, Hagmann CA, Hartemann FV, and Barty CPJ, "Detecting clandestine material with nuclear resonance fluorescence," Journal of Applied Physics 99(2006).
15. Ohgaki H, Daito I, Zen H, Kii T, Masuda K, Misawa T, Hajima R, Hayakawa T, Shizuma T, Kando M, and Fujimoto S, "Nondestructive Inspection System for Special Nuclear Material Using Inertial Electrostatic Confinement Fusion Neutrons and Laser Compton Scattering Gamma-Rays," IEEE Transactions on Nuclear Science 64, 1635–1640 (2017).
16. Hajima R, Hayakawa T, Shizuma T, Angell CT, Nagai R, Nishimori N, Sawamura M, Matsuba S, Kosuge A, Mori M, and Seya M, "Application of Laser Compton Scattered gamma-ray beams to nondestructive detection and assay of nuclear material," European Physical Journal: Special Topics 223, 1229–1236 (2014).
17. Hughes EB, Zeman HD, Campbell LE, Hofstadter R, Meyer-Berkhout U, Otis JN, Rolfe J, Stone JP, Wilson S, Rubenstein E, Harrison DC, Kernoff RS, Thompson AC, and Brown GS, "The application of synchrotron radiation to non-invasive angiography," Nuclear Instruments and Methods in Physics Research 208, 665–675 (1983).
18. Kulpe S, Dierolf M, Braig E, Günther B, Achterhold K, Gleich B, Herzen J, Rummeny E, Pfeiffer F, and Pfeiffer D, "K-edge subtraction imaging for coronary angiography with a compact synchrotron X-ray source," PLOS ONE 13, e0208446 (2018). [PubMed: 30532277]
19. Heck L, Dierolf M, Jud C, Eggl E, Sellerer T, Mechlem K, Gunther B, Achterhold K, Gleich B, Metz S, Pfeiffer D, Kroninger K, and Herzen J, "Contrast-enhanced spectral mammography with a compact synchrotron source," PLoS One 14, e0222816 (2019). [PubMed: 31600236]
20. Kulpe S, Dierolf M, Gunther B, Busse M, Achterhold K, Gleich B, Herzen J, Rummeny E, Pfeiffer F, and Pfeiffer D, "K-edge Subtraction Computed Tomography with a Compact Synchrotron X-ray Source," Sci Rep 9, 13332 (2019). [PubMed: 31527643]
21. Kulpe S, Dierolf M, Günther B, Brantl J, Busse M, Achterhold K, Gleich B, Pfeiffer F, and Pfeiffer D, "Dynamic K-edge Subtraction Fluoroscopy at a Compact Inverse-Compton Synchrotron X-ray Source," Sci Rep 10, 9612 (2020). [PubMed: 32541788]
22. Sun C and Wu YK, "Theoretical and simulation studies of characteristics of a Compton light source," Physical Review Special Topics - Accelerators and Beams 14(2011).
23. Jacquet M and Bruni C, "Analytic expressions for the angular and the spectral fluxes at Compton X-ray sources," Journal of Synchrotron Radiation 24, 312–322 (2017). [PubMed: 28009573]
24. Curatolo C, Drebot I, Petrillo V, and Serafini L, "Analytical description of photon beam phase spaces in inverse Compton scattering sources," Physical Review Accelerators and Beams 20(2017).

25. Paternò G, Cardarelli P, Gambaccini M, and Taibi A, “Dual-Energy X-ray Medical Imaging with Inverse Compton Sources: A Simulation Study,” Crystals 10, 834 (2020).
26. Hwang Y, “Characterization and Applications of Laser-Compton X-ray Source,” Ph.D. thesis (Department of Physics and Astronomy, UC Irvine, 2018).
27. Wang J and Huang W-H, “Spectral distributions of the scattered photons within an acceptance angle in Thomson scattering,” Chinese Physics C 35, 203–208 (2011).
28. Terrall JR, “Elementary Treatment of Relativistic Cross Sections,” American Journal of Physics 38, 14601474 (1970).
29. Wiedemann H, “Equilibrium Particle Distribution,” in Particle Accelerator Physics, 4 ed. (Springer Nature, 2015), pp. 437–457.
30. Effarah H and Reutershan T, “compton-fastfit,” figshare (2022), 10.6084/m9.figshare.19090103.
31. Effarah H, “Data for “Computational method for the optimization of quasimonoenergetic Laser Compton X-ray sources for imaging applications”,” figshare (2022), 10.6084/m9.figshare.19083344.
32. Cardarelli P, Bacci A, Calandrino R, Canella F, Castriconi R, Cialdi S, Del Vecchio A, di Franco F, Drebot I, Gambaccini M, Giannotti D, Loria A, Mettivier G, Paternò G, Petrillo V, Rossetti Conti M, Russo P, Sarno A, Suerra E, Taibi A, and Serafini L, “BriXS, a new X-ray inverse Compton source for medical applications,” Phys Med 77, 127–137 (2020). [PubMed: 32829101]
33. Kulpe S, Dierolf M, Braig EM, Günther B, Achterhold K, Gleich B, Herzen J, Rummeny E, Pfeiffer F, and Pfeiffer D, “K-edge subtraction imaging for iodine and calcium separation at a compact synchrotron x-ray source,” J Med Imaging (Bellingham) 7, 023504 (2020). [PubMed: 32341936]
34. Drebot I, Petrillo V, and Serafini L, “Two-colour X-gamma ray inverse Compton back-scattering source,” EPL 120(2017).
35. Suerra E, Giannotti D, Canella F, Drebot I, Capra S, Cipriani D, Mettivier G, Galzerano G, Cardarelli P, Cialdi S, and Serafini L, “A new method for spatial mode shifting of stabilized optical cavities for the generation of dual-color X-rays,” Nuclear Instruments and Methods in Physics Research Section A: Accelerators, Spectrometers, Detectors and Associated Equipment 1019(2021).

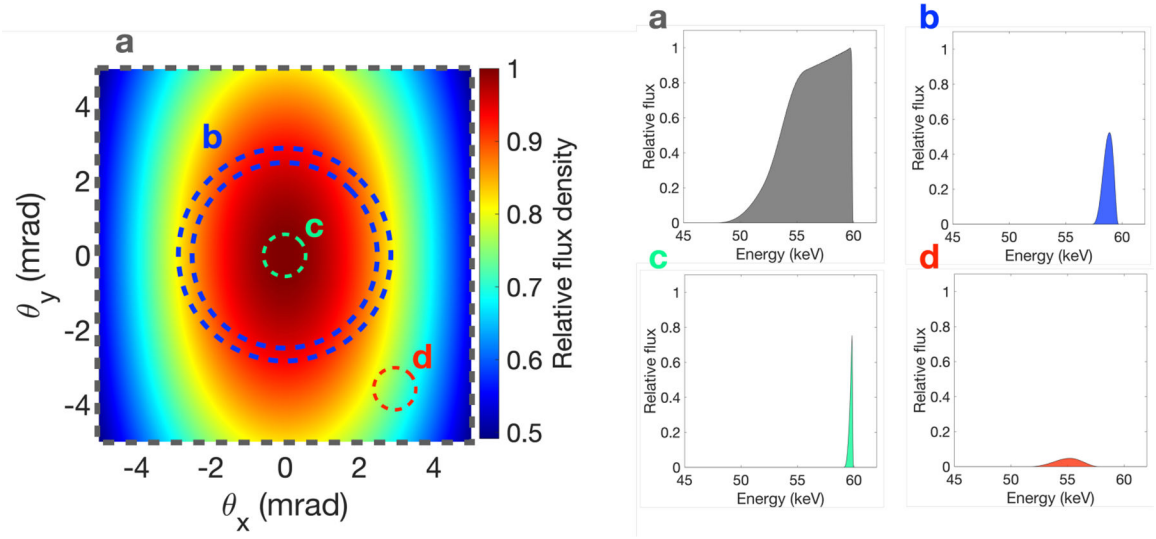


**Fig. 1.**

Visualization of the rich angle-correlated X-ray spectrum of a simulated LCS output with a Compton edge ($E_{CE}$) of 60 keV at observation angles ($\theta_x$, $\theta_y$) up to 5 mrad from the center of the beam profile. On the X-ray flux density plot (left), four regions of interest are highlighted with dashed lines. (a) The entire field of view, (b) a centered annulus, (c) the center, and (d) an off-center region of the LCS X-ray spectrum are highlighted, and the relative total flux and energy spectrum through these regions is illustrated (right). The LCS interaction parameters used to generate these plots are described in more detail in Section 2.1 and are assumed for all LCS X-ray distributions simulated in this paper.

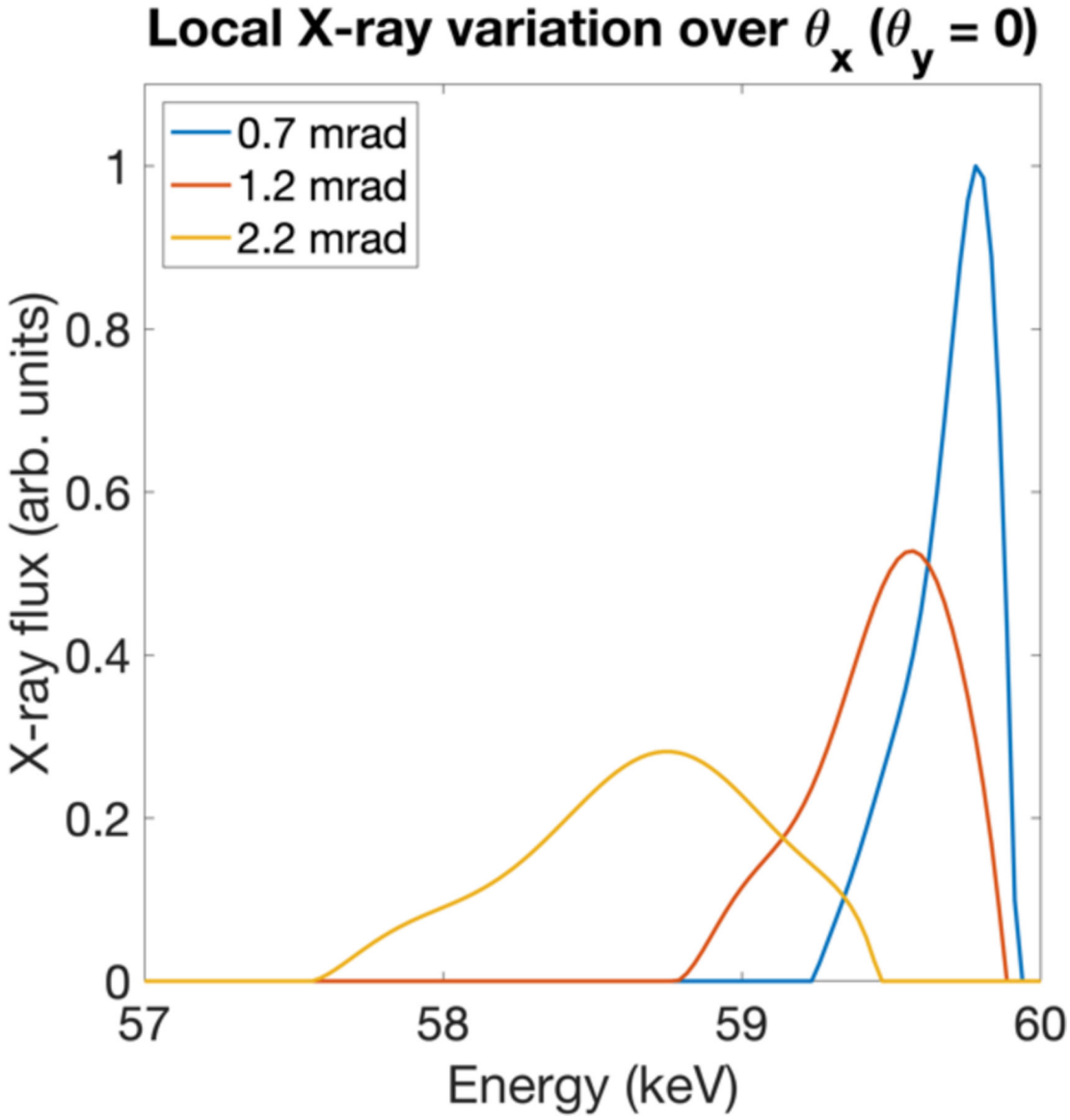


**Fig. 2.**

Visualization of the change in shape of local X-ray distributions as a function of observation angle ($\theta_x$) from an LCS interaction with a Compton edge ($E_{CE}$) of 60 keV.

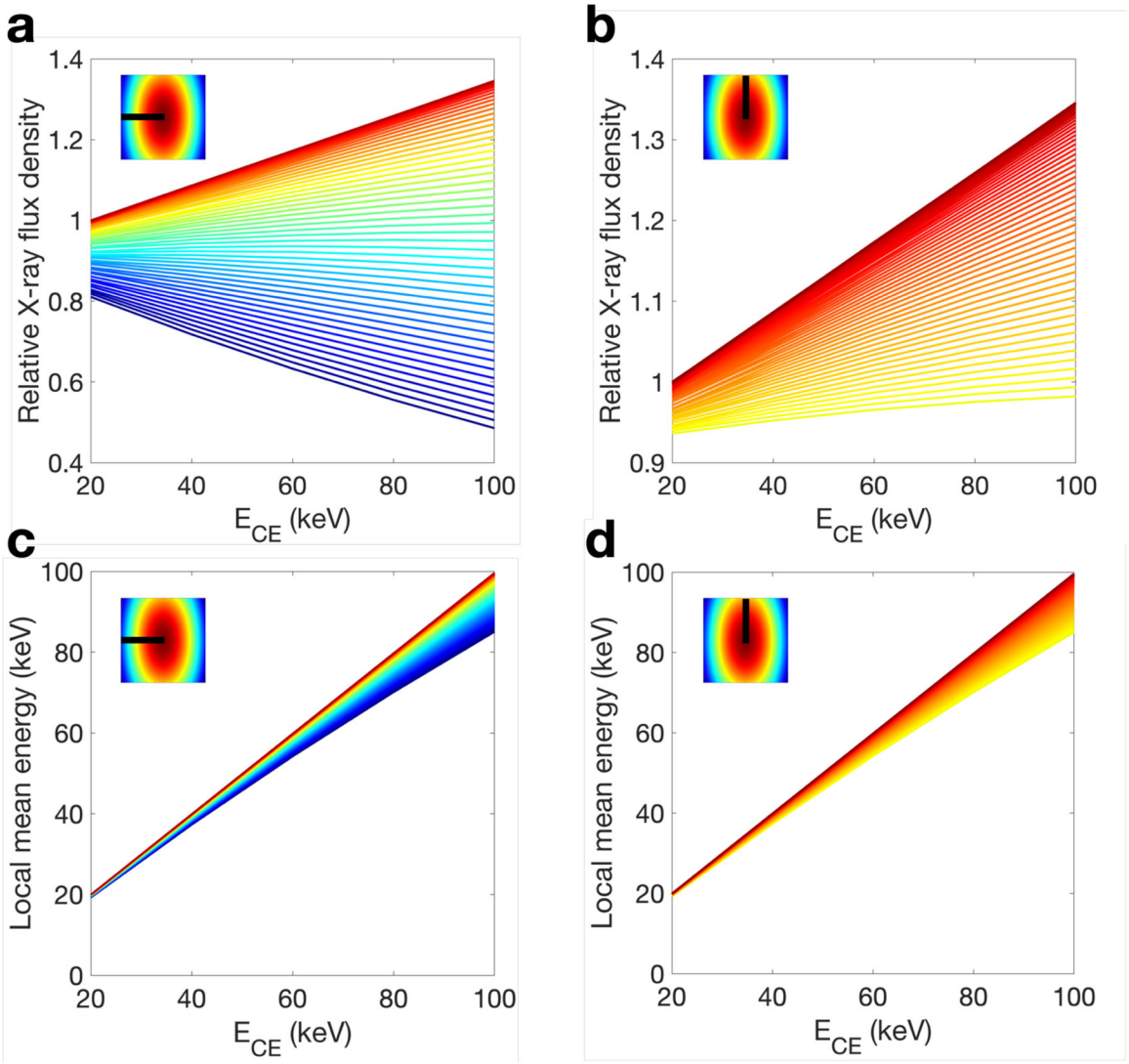


**Fig. 3.**

Change in local X-ray flux density and mean energy at a range of observation angles over a range of $E_{CE}$ values. The color of the plotted line corresponds with the color in the inset X-ray flux density distribution at values overlayed by the black bar in each inset. (a, b) Relative X-ray flux density (normalized to the X-ray flux density at $\theta_x = 0$, $\theta_y = 0$, and $E_{CE} = 20$) for a set of observation angles with (a) −5 mrad < $\theta_x$ < 0 mrad, $\theta_y = 0$ and (b) 0 mrad < $\theta_y$ < 5 mrad, $\theta_x = 0$. (c, d) Mean energy for a set of observation angles with (c) −5 mrad < $\theta_x$ < 0 mrad, $\theta_y = 0$ and (d) 0 mrad < $\theta_y$ < 5 mrad, $\theta_x = 0$.

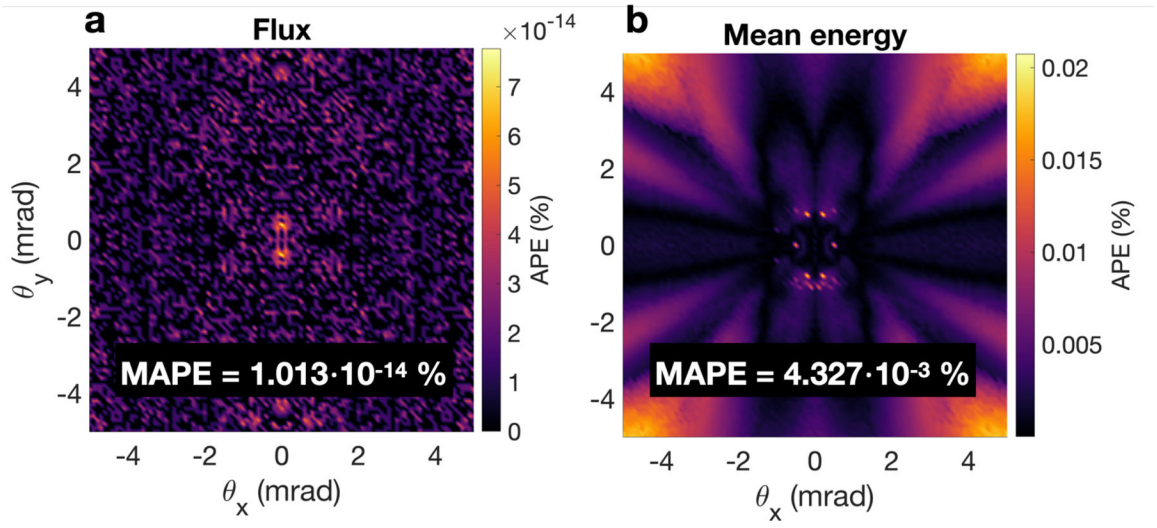


**Fig. 4.**

Image subtraction plots comparing parameters between an LCS X-ray distribution produced through direct LCS simulation and its polynomial approximation using a matrix of eighth degree polynomials. (a) The flux at each observation angle ($\theta_x$, $\theta_y$) has been explicitly constrained to match that of the distribution produced by the LCS code, resulting in a nearly exact match. The deviations between distributions at each observation angle are expressed as an absolute percentage error (APE). (b) The mean energy is compared at each observation angle, with deviations between distributions expressed as an APE. Inset in each image is the mean absolute percentage error (MAPE) over all observation angles.

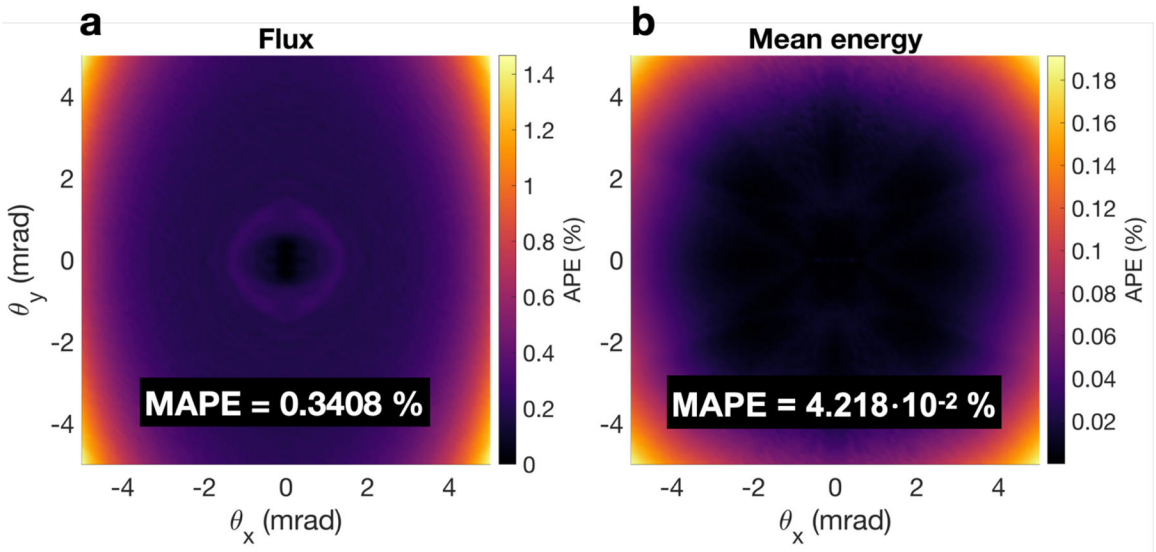


**Fig. 5.**

Image subtraction plots comparing parameters between an LCS X-ray distribution produced through direct LCS simulation and an interpolated LCS X-ray distribution, both with $E_{CE}$ = 80 keV. (a) The X-ray flux is subtracted between interpolated and LCS-interaction-code-generated distributions at each observation angle ($\theta_x$, $\theta_y$). (b) The mean energy, defined to be the mean of the local energy bandwidth, is compared at each observation angle. The deviations between distributions at each observation angle are expressed as an absolute percentage error (APE). Inset in each image is the mean absolute percentage error (MAPE) over all observation angles.

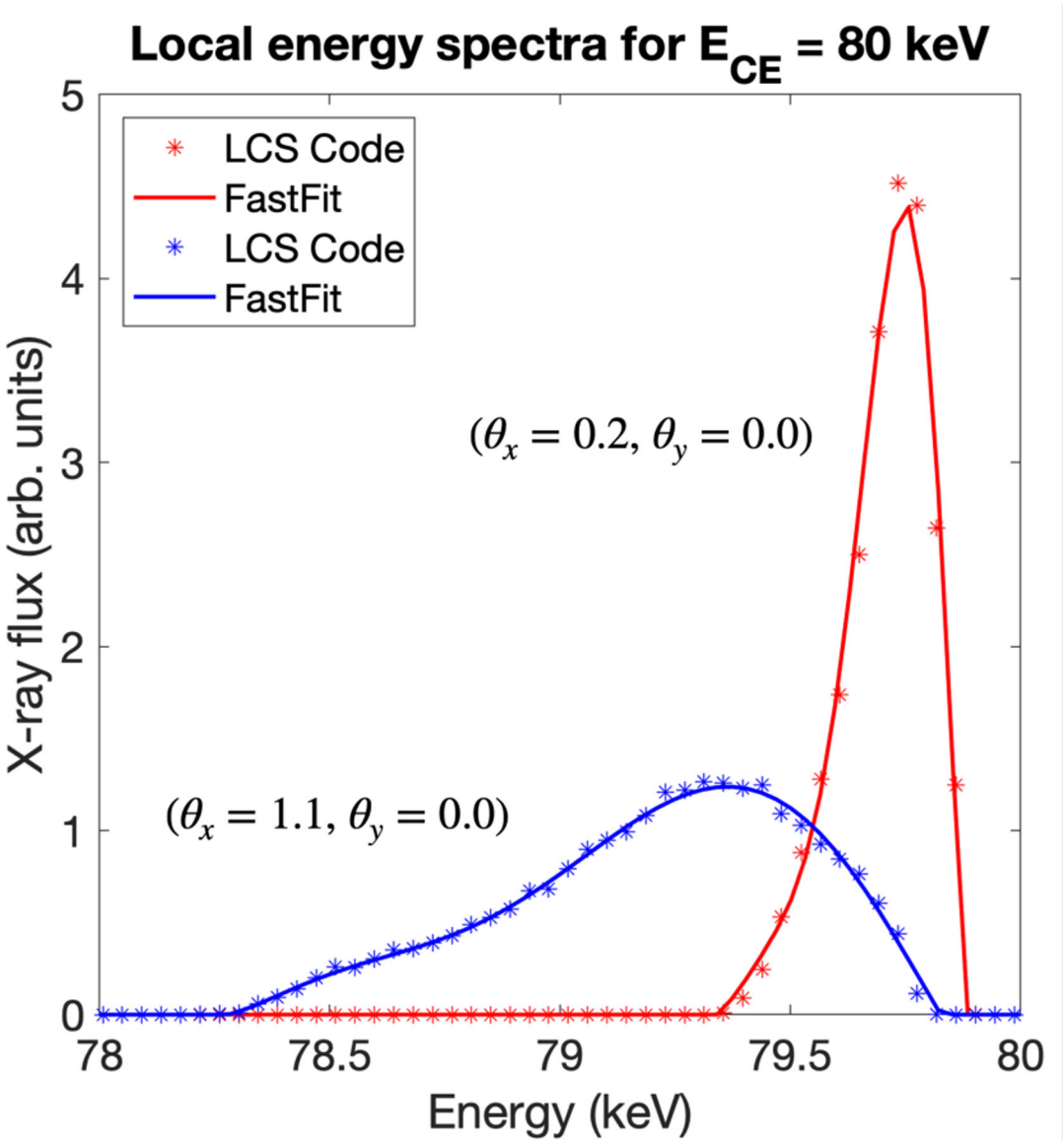


**Fig. 6.**

Comparison of FastFit interpolation and LCS code at two observation angles whose values are in mrad.

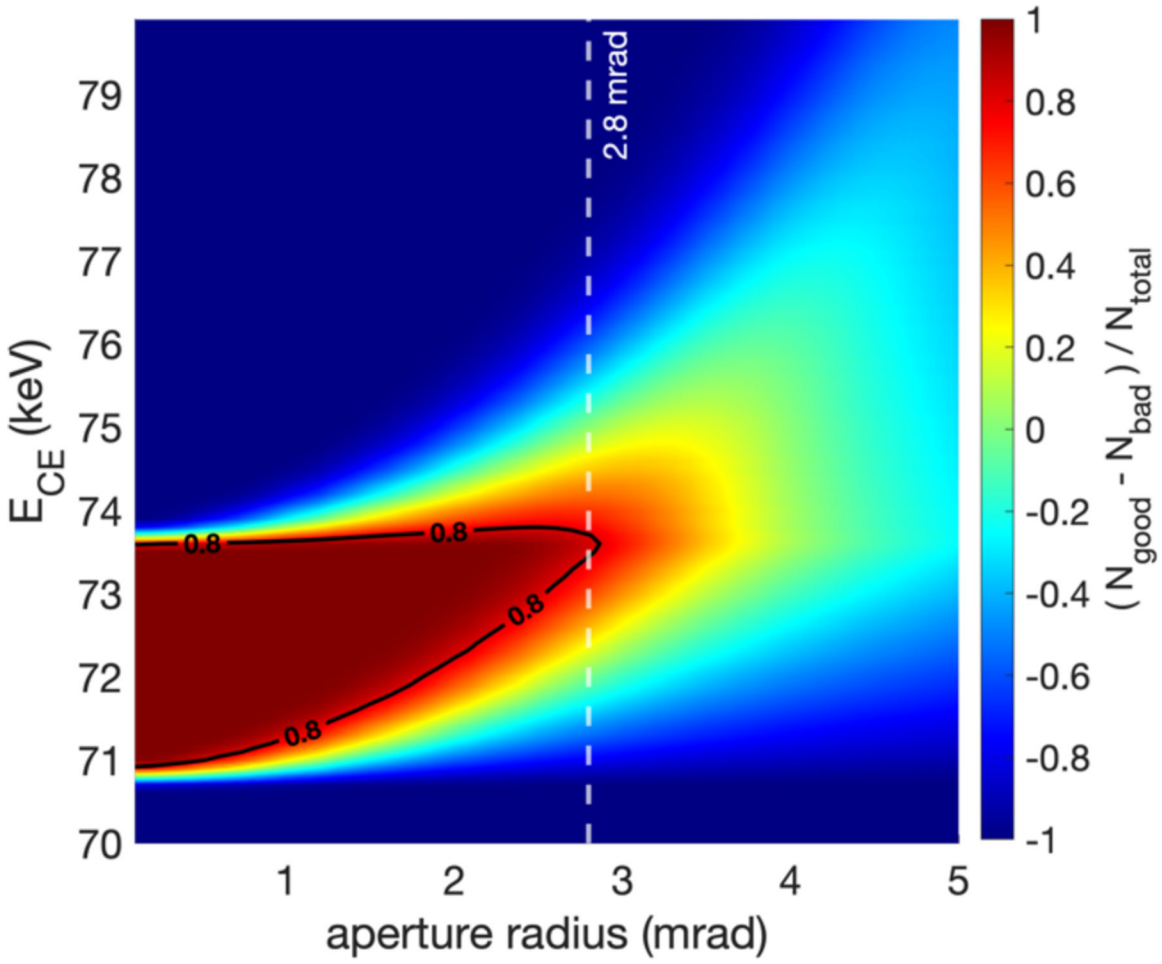


**Fig. 7.**

Optimization of $E_{CE}$ and aperture radius to the X-ray flux passing through the aperture given the energy constraint $E_{good} \equiv 72$ keV ± 2%. A contour line is drawn at $(N_{good} - N_{bad})/N_{total} = 0.8$ to indicate all $E_{CE}$ and aperture radius combinations such that at least 80% of the X-rays that pass through the aperture are within our energy constraint. To maximize the total number of X-rays, we use aperture radius as a proxy for $N_{total}$ and identify our optimal ($E_{CE}$, radius) as (73.6 keV, 2.8 mrad).

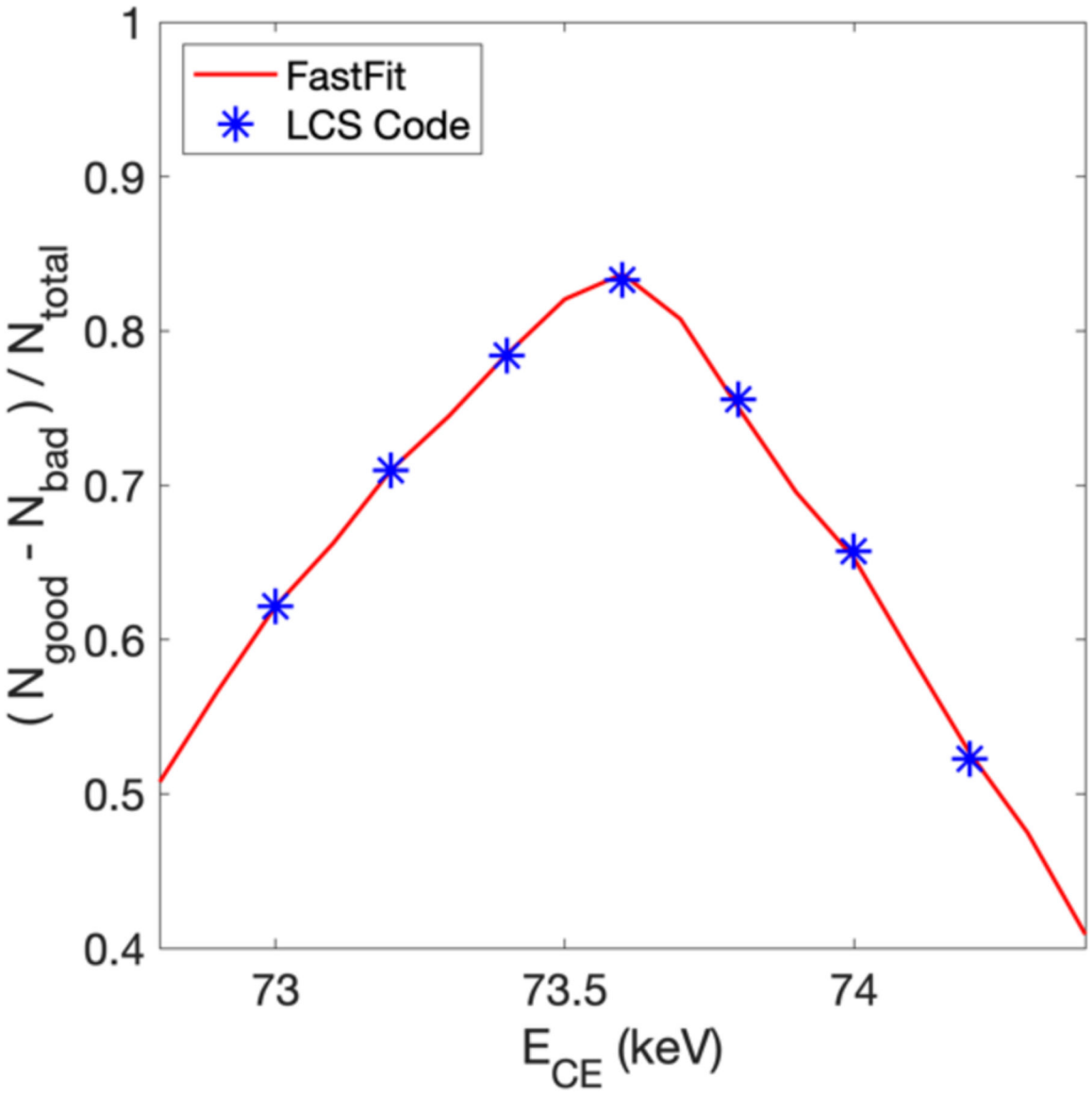


**Fig. 8.**

Evaluating the optimization results for aperture radius and $E_{CE}$ that maximizes the metric $(N_{good} - N_{bad})/N_{total}$ Values for the metric are calculated at a circular aperture radius of 2.8 mrad (indicated by the dotted white line in Fig. 7) for $E_{CE}$ values near the predicted optimal value of $E_{CE} = 73.6$ keV. $N_{good}$ is defined as the X-ray flux within an aperture that falls within a 72 keV ± 2% energy constraint. $N_{bad}$ is defined as all other X-rays within the aperture such that $N_{good} + N_{bad} = N_{total}$.

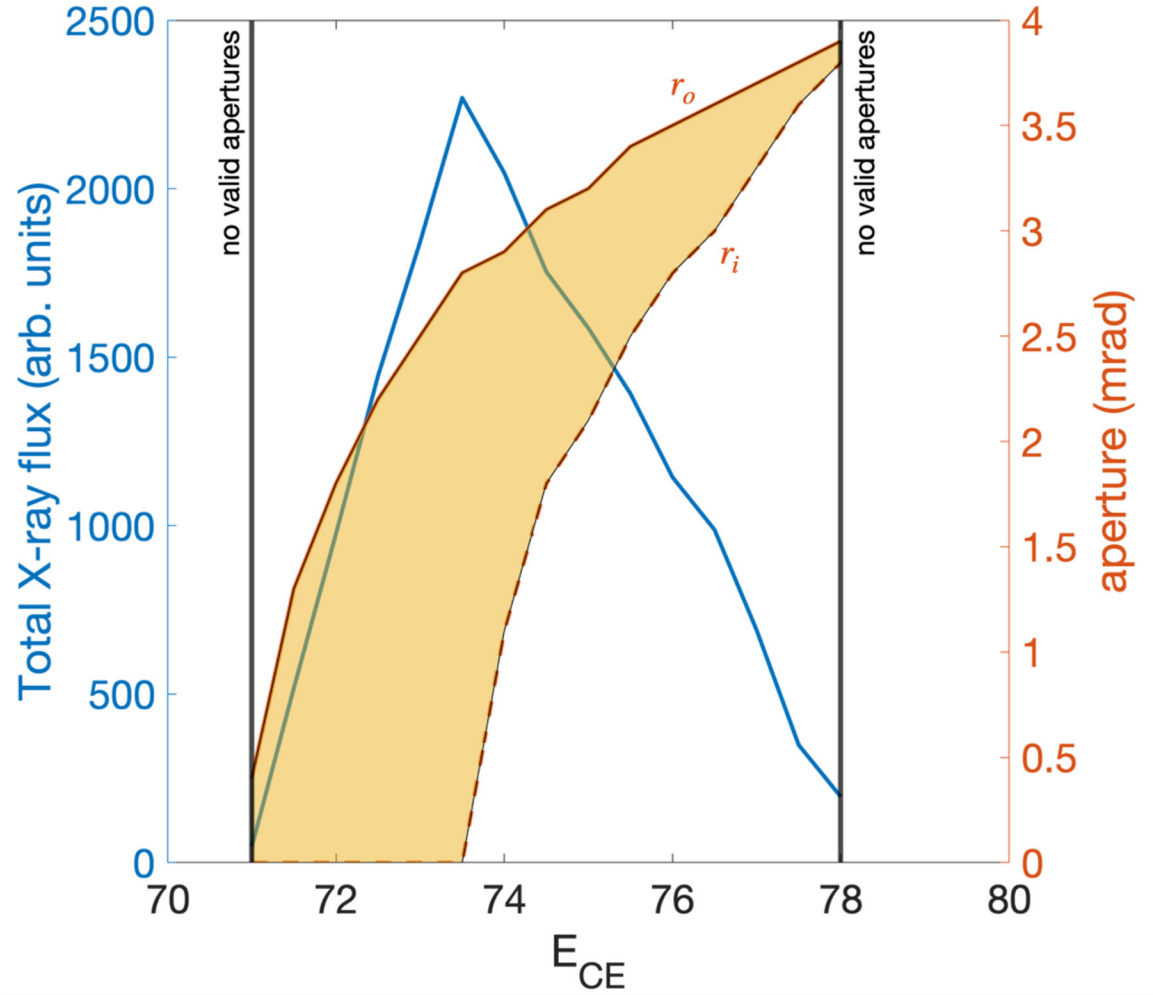


**Fig. 9.**

Finding combinations of $E_{CE}$ and annular aperture radii that maximize X-ray flux through the aperture. At least 80% of X-rays that pass through the aperture must be of energies 72 keV ± 2%. For every $E_{CE}$ examined, the inner ($r_i$) and outer ($r_o$) aperture radii that maximized X-ray flux are reported.

**Table 1.**

MAPE at different $E_{CE}$ values

| | MAPE (%) | |
|---|---|---|
| $E_{CE}$ (keV) | Flux | Mean energy |
| 25 | 0.8015 | 0.08162 |
| 40 | 0.1917 | 0.09486 |
| 55 | 0.07331 | 0.02552 |
| 65 | 0.1430 | 0.01510 |
| 80 | 0.3408 | 0.04218 |
| 95 | 0.09268 | 0.01660 |